Coordination Polymer to Atomically Thin, Holey, Metal-Oxide Nanosheets for Tuning Band Alignment

Sajjad S. Mofarah[1]*, Esmaeil Adabifiroozjaei[2]*, Raheleh Pardehkhorram[3], M. Hussein N. Assadi[4,1], M. Hinterstein[5,1], Yin Yao[6], Xinhong Liu[1], Mohammad B. Ghasemian[7], Kourosh Kalantar-Zadeh[7], Rashid Mehmood[1], Saroj Bhattacharyya[8], Maria Chiara Spadaro[9], Jordi Arbiol[9,10], Sean Lim[6], Yuwen Xu[1], Tohru S. Suzuki[2], Hamidreza Arandyian[11], Pramod Koshy[1]*, and Charles C. Sorrell[1]

[1]   School of Materials Science and Engineering, UNSW Sydney, Sydney, NSW 2052, Australia.
[2]   Research Center for Functional Materials (RCFM), National Institute for Materials Science (NIMS), Tsukuba, Ibaraki 305-0047, Japan.
[3]   School of Chemistry, UNSW Sydney, Sydney, NSW 2052, Australia.
[4]   Center for Green Research on Energy and Environmental Materials (GREEN), National Institute for Materials Science (NIMS), 1-1 Namiki, Tsukuba, Ibaraki 305-0044, Japan.
[5]   Institute for Applied Materials, Karlsruhe Institute of Technology, 76131 Karlsruhe, Germany.
[6]   Electron Microscopy Unit (EMU), Mark Wainwright Analytical Centre, UNSW Sydney, Sydney, NSW 2052, Australia.
[7]   School of Chemical Engineering, UNSW, NSW 2052, Australia.
[8]   Mark Wainwright Analytical Centre, UNSW Sydney, Sydney, NSW 2052 Australia.
[9]   Catalan Institute of Nanoscience and Nanotechnology (ICN2), CSIC and BIST, Campus UAB, Bellaterra, 08193 Barcelona, Catalonia, Spain.
[10] ICREA, Pg. Lluís Companys 23, 08010 Barcelona, Catalonia, Spain.
[11] Laboratory of Advanced Catalysis for Sustainability, School of Chemistry, The University of Sydney, Sydney 2006, Australia.

*Correspondence to: s.seifimofarah@unsw.edu.au, adabifiroozjaei.e@nims.go.jp, koshy@unsw.edu.au
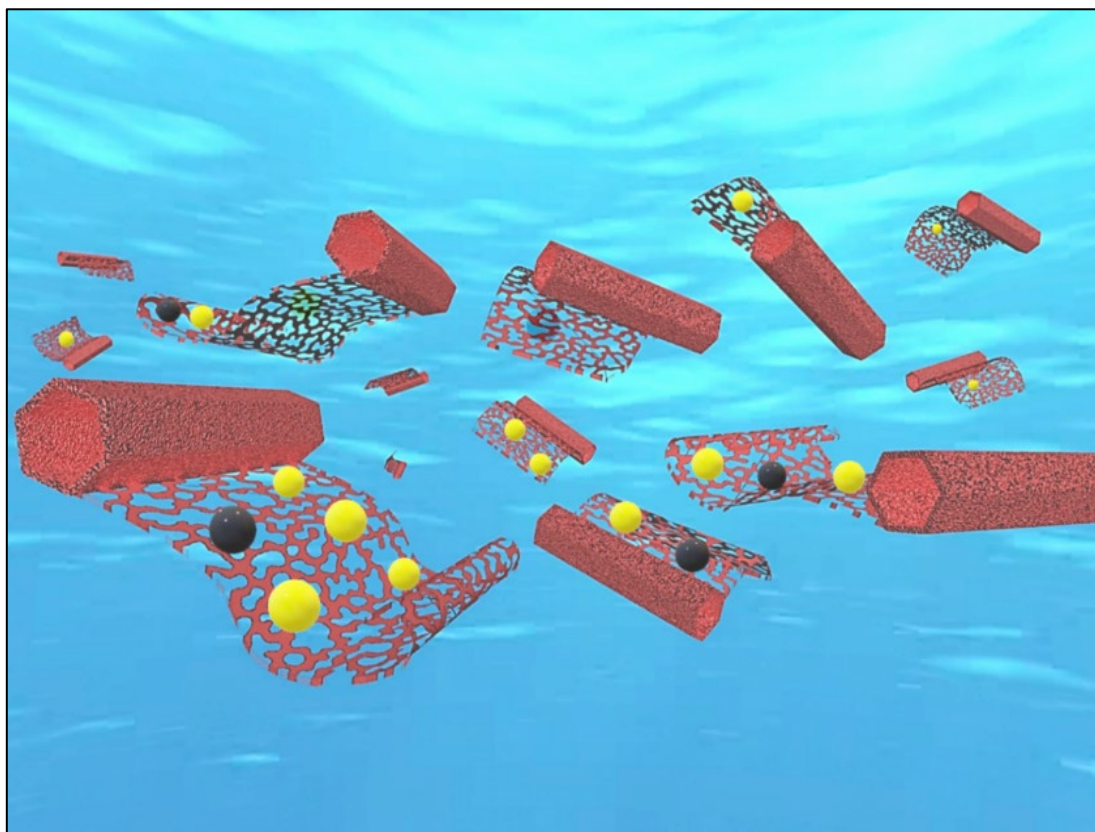
Abstract

Although two-dimensional (2D) nanostructures hold considerable fundamental and applied potential, irreversible restacking and complicated fabrication strategies have limited their uses in energy and environmental applications. Here, we report a versatile strategy to fabricate a new class of atomically thin nanostructures with mosaic-like architectures, containing nanoholes. The fabrication process involves rapid exfoliation of stratified metal-based coordination polymers in water at room temperature, which was used to synthesize ultrathin CeO_2, TiO_2, and ZrO_2 nanosheets with minimal lateral and transverse charge carrier diffusion distances. Additionally, we illustrate a simplified method to fabricate mixed 0D/2D heterojunction nanostructures of 0D transition metal oxides (TMOs) and 2D holey nanosheets with electronic structures modified by band alignment rearrangement. The capacity to engineer the band positions establishes a route to optimize photocatalysts for specific applications. This strategy offers a cost-effective, high yield, room temperature, and template-free approach to fabricate functional holey 2D nanostructures for a wide range of energy and environmental applications.

Ultrathin 2D nanomaterials exhibit unique chemical and electronic properties that are absent in other-dimensional nanostructures[1],[2]. This effect arises from their high surface-to-volume ratio, where nearly all ions are available for reactions/interactions, thereby making the nanostructures ideal for surface-dependent applications, *e.g.,* energy[3] and catalysis[4]. 2D nanostructures generally are synthesized using three main strategies, *viz.,* top-down (exfoliation)[5], bottom-up[6], and liquid metal touch-printing[7]. The top-down technique involves exfoliation of bulk structures into pristine nanosheets (no voids) and so is limited to only materials with intrinsically layered structures[5b, 8]. The other two strategies generally are associated with the challenges of low yields[9], procedural complexities[10], and/or necessity of high temperatures[11]. Therefore, there is an imperative to develop simplified, scalable, and cost-effective strategies to synthesize 2D architectures with high densities of defects. One such strategy lies in 2D mosaic structures since the grain misalignment not only increases the density of the active sites (defects) at the grain boundaries but also prevents epitaxial restacking[12]. This strategy can be improved further by the creation of voids in the 2D nanostructure[13], which can increase the density of accessible active sites at the newly exposed surfaces. Although holey 2D graphene nanostructures have been studied previously[14], there is very limited work on the synthesis of holey 2D metal oxides (MOs), including the discontinuous deposition of metal oxides on surface-modified graphene as a sacrificial template[15]. Holey 2D transition metal chalcogenides (TMCs) and selenides (TMS) also have been fabricated by etching of continuous transition metal oxide (TMO) nanosheets[16]. While these approaches resulted in enhanced performance, the processes were relatively complex, including the requirement of a surfactant, a sacrificial template, and/or an additional step for removal of the template by high-temperature processing, which ultimately resulted in nanosheet thicknesses tens of nanometres[17]. The present work demonstrates an alternative and adaptable strategy to create holey 2D nanostructures of MOs at room temperature without the use of a template. This technique is based on the rapid exfoliation of bulk-layered, metal-based, coordination polymers (MCPs) into monolayers in aqueous solution, followed by transformation

into holey 2D MO nanostructures of thickness of two-unit cells (~1.1 nm for CeO_2) but lateral sizes in the centimetre scale. The versatility of the method is confirmed through the synthesis of similar structures for TiO_2 and ZrO_2. Further, broad applicability of this strategy is illustrated through the synthesis of mixed 0D/2D heterojunction nanostructures of TMO (0D) and CeO_{2-x} (2D). These nanostructures exhibit modified electronic structures derived from the rearrangement of the band alignments owing to the presence of the TMOs. The holey CeO_{2-x}-based heterojunction nanostructures show very high photocatalytic activity under simulated solar light. Therefore, this study propose a new direction towards synthesis of extremely-thin holey 2D nanostructures, which can be used to many catalysis and energy storage applications.

A novel cerium-based coordination polymer (Ce-CP) with bulk-layered structure was synthesised by modified anodic electrochemical deposition. Figures 1(a)-(d) show a schematic of the Ce-CP hexagonal tube exfoliation in deionized (DI) water. These schematics are based on transmission electron microscopy (TEM) images obtained after 2, 4, 6, and 8 min ultrasonication, as shown in Figures 1(e)-(h), respectively. Details of the Ce-CP formation process are provided in Supplementary Note 2. In the lack of reference data consistent with the X-ray diffraction (XRD) pattern obtained for the Ce-CP, the corresponding crystal structure was investigated by comparing *ab-initio* molecular dynamics simulations with XRD and neutron diffraction patterns; the results are given in Supplementary Note 3. The stratified Ce-CP crystal structure is illustrated in Figure 1(i), left, where the interlayer spaces are mutually bonded by weak van der Waals (vdW) forces between intercalated protons and the terminating chlorine ions of the bidentate trichloroacetate (TCA) ligands.
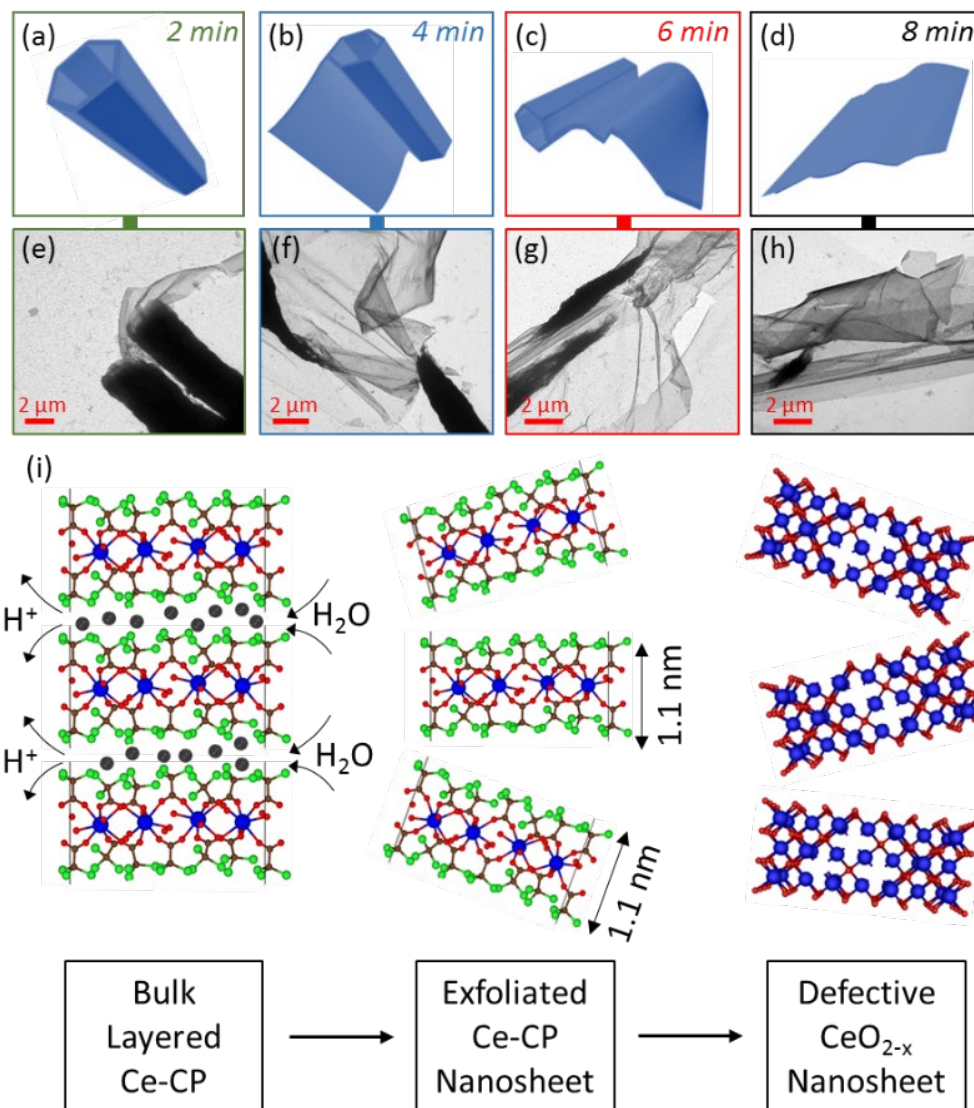
Figure 1. Exfoliation of Ce-CP hexagonal nanotube into 2D nanostructures. (a-d) schematic of Ce-CP exfoliation, (e-h) *ex-situ* TEM images following water exfoliation of the Ce-CP hexagonal nanotube at room temperature, (i) schematic of layered structure of Ce-CP and penetration of water molecules between stacked Ce-CP nanosheets, resulting in transformation of Ce-CP nanosheets into defective CeO_{2-x} nanosheets in basic aqueous solution. Blue, green, red, brown, and black balls represent cerium, chlorine, oxygen, carbon, and hydrogen ions, respectively. Gaps within the defective CeO_{2-x} nanosheet represent oxygen vacancies.

Applying ultrasonication to the Ce-CP tubes it is possible to enhance the exfoliation through the vibration's breakage of the vdW bonding and resultant facilitated water molecule penetration (Figure 1(i), center). Further, the *c*-axis lattice parameter of the Ce-CP crystal structure was measured to be 1.1 nm (see supplementary Note 3), which represents the thinnest possible Ce-CP nanosheet, *i.e.*, a Ce-CP monolayer. Upon exposure to DI water of high pH, the Ce-CP nanosheets transform readily into defective CeO_{2-x} nanosheets, as shown schematically in further stage of Figure 1(i), right.

Morphological and structural characterization data for the formation of the Ce-CP and CeO_{2-x} nanosheets are shown in Figure 2. Scanning electron microscopy (SEM) and TEM images of free-standing Ce-CP hexagonal

nanotubes shown in Figure 2(a) and (b), respectively. The critical role of oxygen evolution during water hydrolysis and the consequent formation of protons during the Ce-CP nanotube synthesis were elucidated by thermodynamic and aqueous chemistry analyses given in Supplementary Note 4. The polycrystalline nature of the Ce-CP nanotubes is shown in the rings in the selected area electron diffraction (SAED) patterns shown in the inset of Figure 2(b). The SAED results are consistent with the XRD pattern (Figure 2(c)), which is indexed to the triclinic system, space group P$\bar{1}$, with a = 1.31 nm, b = 1.32 nm, c = 1.10 nm, α = 81.20°, β = 93.21°, γ = 112.93°. The data describing the crystallography of the Ce-CP, which has been determined to be $Ce(TCA)_2(OH)_2 \cdot 2H_2O$, are given in Supplementary Note 3.
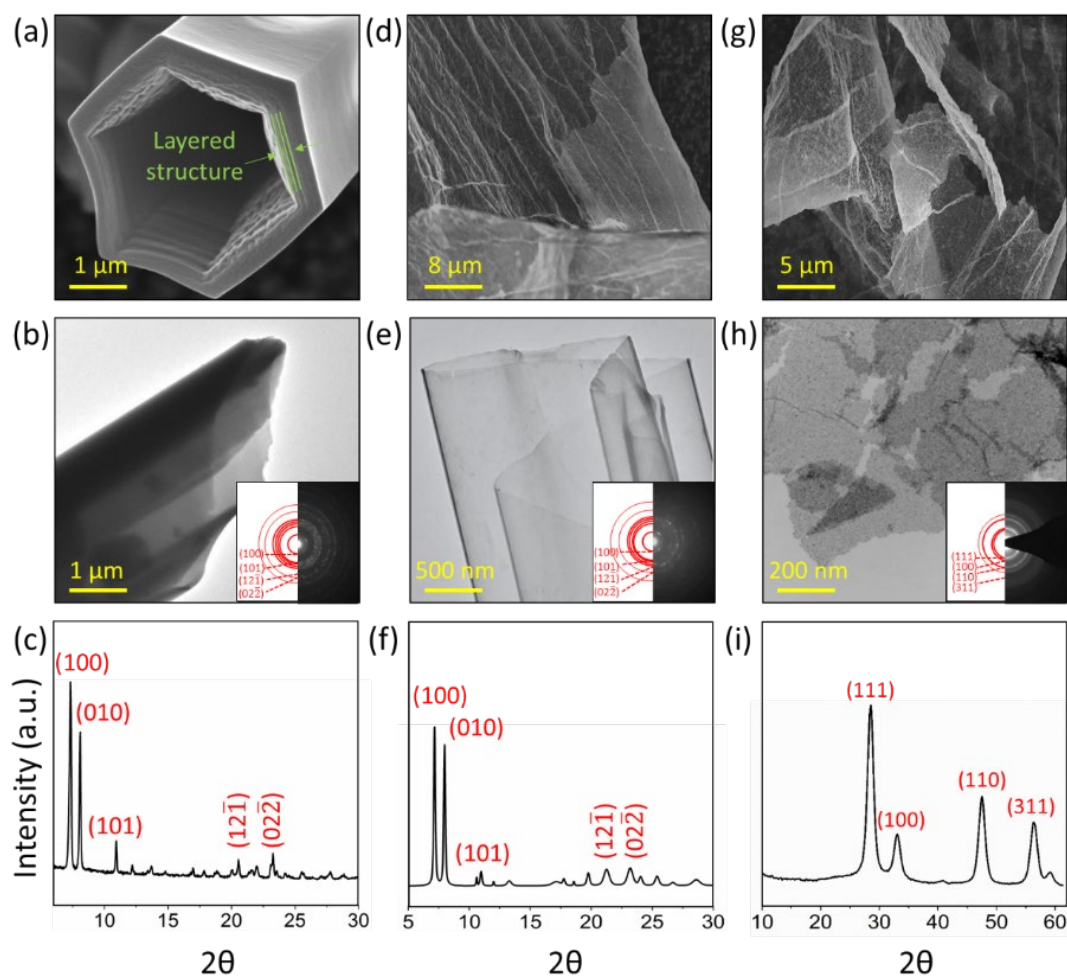

Figure 2. Structural and morphological evolution of Ce-CP hexagonal nanotube into CeO_{2-x} nanosheets. (a) SEM image of Ce-CP hexagonal nanotube, (b) TEM image of Ce-CP hexagonal nanotube (inset: SAED pattern), (c) XRD pattern of Ce-CP hexagonal nanotube, (d) SEM image of Ce-CP nanosheet, (e) TEM image of Ce-CP nanosheet (inset: SAED pattern), (f) XRD pattern of Ce-CP nanosheet, (g) SEM image of holey CeO_{2-x} nanosheet, (h) TEM image of holey CeO_{2-x} nanosheet (inset: SAED pattern), (i) XRD pattern of CeO_{2-x} nanosheet.

Figures 2(d) and (e) show SEM and TEM images of micron-scale nanosheets obtained by exfoliation of the Ce-CP hexagonal nanotube in DI water at room temperature. However, both the SAED (Figure 2(e), inset) and XRD data (Figure 2(f)) reveal no changes in the crystal structure, thus confirming the retention of the $Ce(TCA)_2(OH)_2 \cdot 2H_2O$ following exfoliation.

The final steps of the process involve increasing the pH of the solution to pH = 8, during ultrasonication, leading to dissolution of the TCA from the two surfaces (Figure 1(i), left). Consistent with the Pourbaix diagram for Ce(III)/Ce(IV) system[18], this process leaves a highly reactive interior M-OH ($Ce(OH)_2^{2+}$) substructure intact, which rapidly converts to the more stable $Ce(OH)_4$ followed by the rapid formation of stable CeO_{2-x}. This mechanism allows the Ce-CP nanosheet morphology to be converted to CeO_{2-x} (Figure 2(g)) in the cubic fluorite structure (space group Fm3m[19]), without affecting the Ce-OH-based substructure, as confirmed by SAED (inset Figure 2(h) and XRD (Figure 2 (i)). In order to confirm removal of the TCA, energy dispersive spectroscopy (EDS) elemental mapping was carried out for both Ce-CP nanosheet and CeO_{2-x} nanosheet, as shown in Supplementary Figure S18 and S19, respectively. The rapid evolution of Ce-CP into CeO_{2-x} also is shown by *in situ* laser Raman microspectroscopy of nanosheets subjected to an alternative removal method. Supplementary Figure S20 reveals the removal of the organic-related peaks as a function of ultrasonication time and application of heat at 100˚C and the simultaneous increase in the intensity of asymmetric CeO_2-related-peak (F_2g vibration mode) at ~457 cm^{-1}. Assigning the remaining Raman peaks confirms the chemical rearrangement of the Ce-CP into CeO_{2-x}. The simplified and rapid formation of the holey nanosheet delivers a defect-rich CeO_{2-x} structure. Thermodynamic analysis of the Ce(III) and Ce(IV) species suggests that this rapid transformation is due to the high field strength of Ce(IV) over a wide pH range and thus a correspondingly the strong affinity for CeO_{2-x} formation[20] shown in the corresponding Pourbaix diagram (Supplementary Figures S17).

It is significant that, during the transformation process of the Ce-CP nanosheets to CeO_{2-x} nanosheets, high densities of nanoholes across the ultrathin sheets are formed as shown in Figure 2(h). The high-angle annular dark field (HAADF) STEM images of the holey CeO_{2-x} nanosheets are shown in Figures 3(a-c); here single crystallites of lateral sizes in the range 3-6 nm intersect to create nanoholes at the multiple grain boundary junctions owing to imperfect nanosheet packing. Similar to the work of Yu *et al.*[13a, 15b], the conclusion of strong chemical bonding between the crystallites is supported by the apparent intergrowths at the grain boundaries, despite their high angles, as suggested by merged lattice fringes (Supplementary Figure S21). The constraint of the crystallites to 2D is important because this facilitates perfect lattice correspondence by symmetric atomic registry of the cubic oxide lattices across the interface, regardless of grain boundary angle. This unusual condition enables the self-assembly of large, ultrathin, polycrystalline MCP nanosheets, regardless of orientation, where the M-OH substructures, act as nodes, attain atomic registry and the organic linkers contribute to bridge the nodes. However, as the individual nanosheets have irregular outlines, nanoholes are formed when atomic registry is not possible. The presence of such holes in 2D nanostructures has been reported to improve dramatically their functionalities owing to the introduction of exposed surfaces, increased density of surface defects, and improved accessibility of these active sites through shortening of the lateral charge carrier diffusion path[13b, 21]. A high density of defects in the CeO_{2-x} nanosheets is illustrated by electron energy loss spectroscopy (EELS), as shown in Figures 3 (d) and (e). The EELS data show that $V_O^{\bullet\bullet}$ are present both on the grain boundaries (Figure 3(d)) and within the CeO_{2-x} crystallites (Figure 3(e)). The intensity ratio of the M_5 (3d 5/2 → 4f 7/2) and M_4 (3d 3/2 → 4f 5/2) peaks are known to show a linear relationship, where the higher ratio

indicates higher $[V_O^{\bullet\bullet}]$[22]. The EELS data allow determination of the $[V_O^{\bullet\bullet}]$ from the ratio of the M_5 (orange) and M_4 (green) peaks, where the ratios for minimal $[V_O^{\bullet\bullet}]$ (0 at% for stoichiometric $CeO_{2.0}$) and maximal $[V_O^{\bullet\bullet}]$ (25 at% for $CeO_{1.5}$) are ~0.9 and ~1.25, respectively. The EELS data indicate a $[V_O^{\bullet\bullet}]$ of 0.95 within the crystallite and 1.15 at the interface of two crystallites. While the higher $[V_O^{\bullet\bullet}]$ at the crystallite interface is as expected[23], the presence of $V_O^{\bullet\bullet}$ within the crystallite has been recently reported[20b]. The formation of such defects is likely to result from the low energy required to transform Ce-CP into CeO_{2-x} in aqueous solution at room temperature and the consequent imperfect recrystallization.
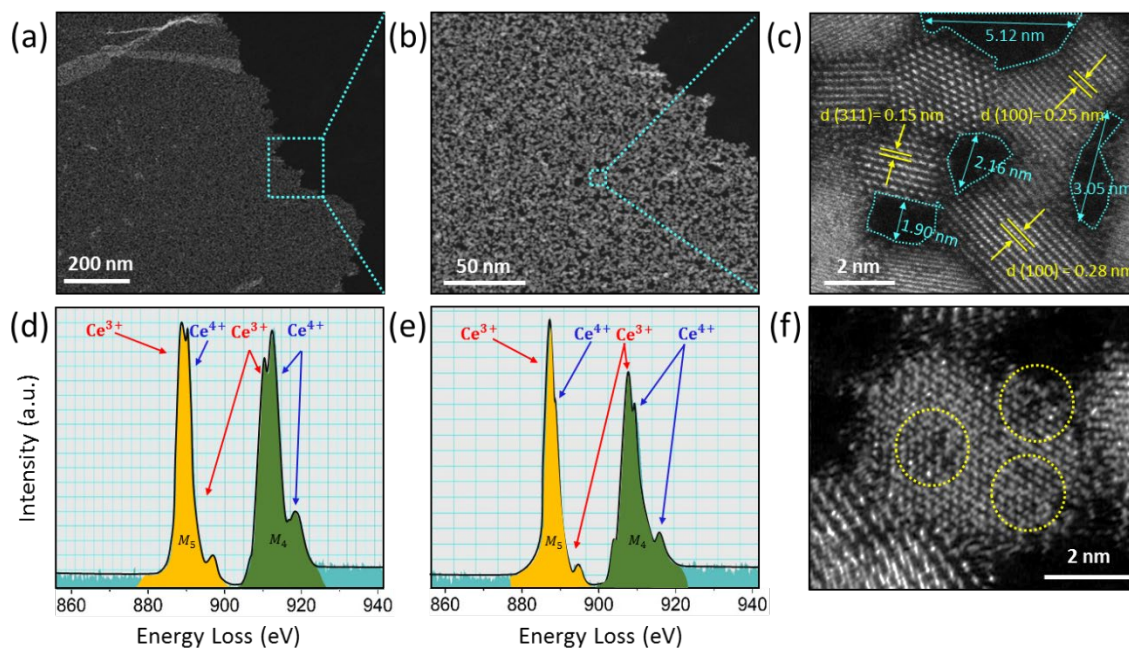

Figure 3. Defect and structural analysis of CeO_{2-x} holey nanosheets. (a,b) Low-magnification HAADF image of CeO_{2-x} nanosheets, (c) High-magnification HAADF image of CeO_{2-x} nanosheets illustrating nanoholes of ~2-5 nm lateral size, (d) EELS spectra from an intercrystallite region in CeO_{2-x} nanosheets, (e) EELS spectra from within a CeO_{2-x} crystallite, (f) High-magnification HAADF image showing Ce vacancies within a CeO_{2-x} crystallite.

It is notable that the high-magnification HAADF image of the holey nanosheet (Figure 3 (f)) indicates the presence of Ce vacancies (V_{Ce}''''), which, to the best of our knowledge, do not appear to have been reported for CeO_2-based materials. This defect may indicate Schottky pair formation, which requires ~2-3 eV more than that required for O vacancy formation[24]. Nonetheless, this may be compensated by the short diffusion distances (lateral and transverse) in the nanosheets. Both the HAADF imaging and EELS analysis in STEM mode were conducted while the samples were cooled *in situ* to liquid nitrogen temperature in order to avoid the creation of artefact vacancies from the high vacuum and/or electron beam irradiation[25].

The use of Ce-CP as sole precursor in the absence of a template, surfactant, etching or other technical complexities to synthesize holey CeO_{2-x} nanosheets represents a simplified fabrication approach requiring effectively only an electrochemical setup Critically, the high yield of the process is demonstrated by the synthesis of large amounts of holey CeO_{2-x} nanosheets in a single batch, as shown in Supplementary Figure S22,

in which the lateral size of the nanosheets, which are reversibly stacked by van der Waals bonding, is as large as 30 mm.

Furthermore, the flexibility of the fabrication method is confirmed by the syntheses of a layered titanium-based CP (Ti-CP) and a zirconium-based CP (Zr-CP). Details of the morphological and structural characterization of these bulk layered MCPs are given in Supplementary Note S6. Similarly to Ce-CP, the Ti-CP and Zr-CP were exfoliated rapidly in basic aqueous solutions into nanosheets, as illustrated by TEM and EDS analyses (Supplementary Note S7). The morphological analyses of CeO_{2-x}, TiO_{2-x}, and ZrO_{2-x} nanosheets are shown in Figures 4(a-c), respectively, where TEM images reveal the holey nanostructures of the MCP-derived MOs. Also, Figures 4(d-f) show SAED patterns of the randomly-oriented polycrystalline nanosheets indexed to CeO_2, TiO_2, and ZrO_2, respectively. Considering the ultrathin nature of the holey nanosheets, surface chemical analysis effectively provides bulk analysis since the penetration depth of XPS is ~3 nm[26]. As an example, quantitative analysis of CeO_{2-x} (Supplementary Figure S42) was carried out by deconvolution of Ce $3d$ orbital of XPS spectra revealing significant Ce^{3+} concentrations, which generally are associated with corresponding oxygen vacancy concentrations ($[V_O^{\bullet\bullet}]$) through charge compensation[27]. These results are in agreement with the EELS data shown in Figure 3 (d) and (e).

In order to measure the thicknesses of the holey MO nanosheets, atomic force microscopy (AFM) imaging was done by deposition of the nanosheets onto silicon substrates, as shown in Figures 4(g-i), using the van der Walls printing method[7b, 28]. The corresponding height-profiles are shown by the two step-heights from the substrate in Figures 4(j-l). For CeO_{2-x}, these are 1.1 nm and 1.2 nm, indicating that the nanosheets are of 2 unit cell thickness (CeO_2 unit cell = 0.54 nm[29]). The thicknesses of the TiO_{2-x} and ZrO_{2-x} nanosheets were measured to be ~10.0 nm and ~1.8 nm, respectively, indicating thicknesses of 20-40 and 3-4 unit cells, respectively. The thickness of the TiO_{2-x} nanosheet is likely to be due to the poor packing arising from the anisotropy of the tetragonal anatase[30] while the thin ZrO_{2-x} nanosheet probably resulted from the effectively equiaxed lattice[31]. These data suggest that self-assembled MOs of equiaxed or possibly highly anisotropic and hence self-aligned nanostructures are more likely to yield ultrathin nanosheets.
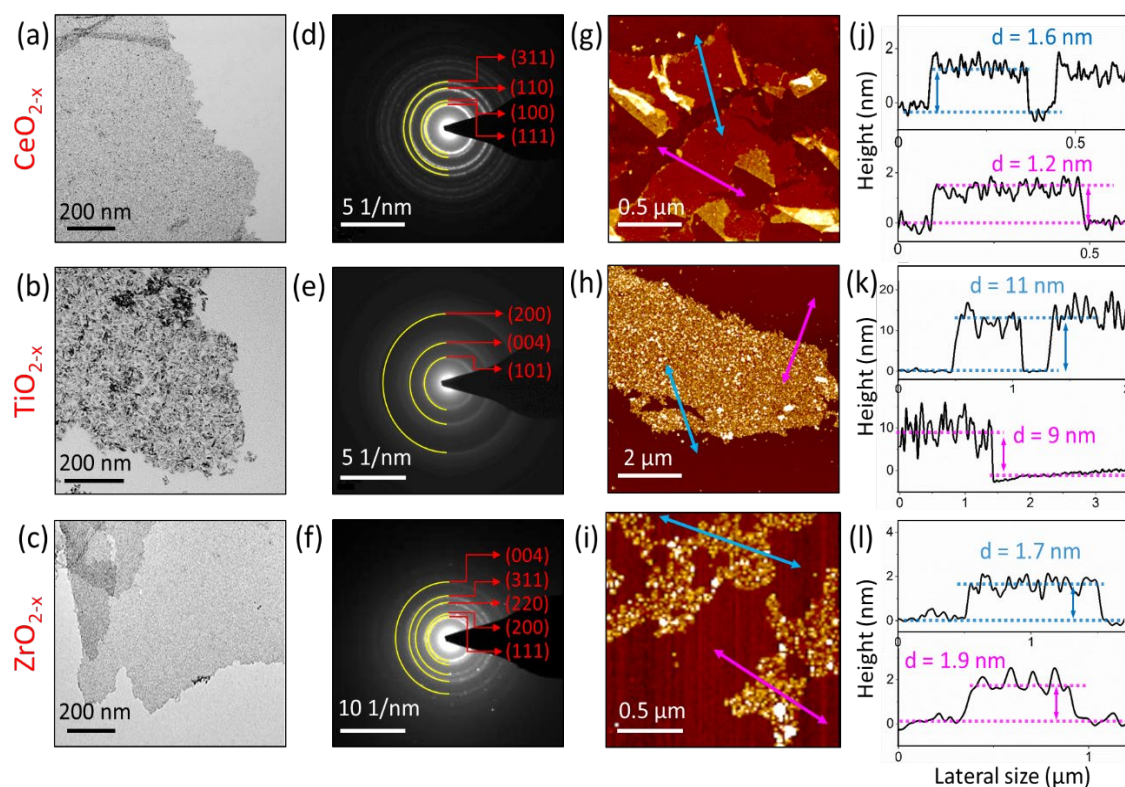
Figure 4. Characterization of holey MO nanosheets. (a) TEM image for CeO_{2-x} nanosheet, (b) corresponding SAED pattern, (c) AFM image, and (d) corresponding height profile; (e) TEM image for TiO_{2-x} nanosheet, (f) corresponding SAED pattern, (g) AFM image, (h) corresponding height profile; (i) TEM image for ZrO_{2-x} nanosheet, (j) corresponding SAED pattern (k) AFM image, and (l) corresponding height profile.

The applicability for holey CeO_{2-x} nanosheets can be broadened by their use as a template in the fabrication of mixed 0D/2D heterojunction nanostructures with Fe-, Ni-, and Zn-based TMOs (0D). Using the general synthesis platform, the holey CeO_{2-x} nanosheets were dispersed in an aqueous solution (pH = 6), which yielded a relatively stable suspension with zeta potential of -25 mV (Supplementary Figure S43), slightly lower than the conventional threshold for stability (-30 mV[32]). In addition, considering the speciation diagrams for the TM ions (Supplementary Figure S44), the predominant species, within the acidic pH of CeO_{2-x} suspension, are expected to be TM^{n+}. Therefore, this situation establishes electrostatic attraction between the positively charged metal species and the negatively charged holey nanosheets, thereby providing the mechanism for the assembly of metal species on the nanosheet surfaces[33]. This is demonstrated by the reductions in the zeta potential to -20 mV, -19 mV, and -14 mV for the Fe, Ni, and Zn heterostructure suspensions, respectively (Supplementary Figure S45). This approach can significantly increase the nanosheets functionalities by preventing the layers from stacking during minimization of the interplanar van der Waals (vdW) interactions and by maximizing the accessibility of the active sites[34]. Moreover, the mixed 0D/2D heterostructures provide sufficient hybridization between the atomic orbitals, enhancing carrier delocalization at the junction interfaces[34]. The elemental, mineralogical, and crystallographic investigations of the heterostructures were carried out by EDS, laser Raman microspectroscopy, and XRD as shown in Figure 5. The formation of the heterojunction nanostructures were shown by nanosheets EDS mapping in Figures 5(a-c) revealing a homogenous distribution of 0D TMOs. The

coexistence of the TMOs and CeO_{2-x} was confirmed by the laser Raman microspectra (Figures 5(d-f)). Since the peak for pristine CeO_2 is at 464 cm^{-1}, the large peaks at ~460 cm^{-1} for FCO, NCO, and ZCO (assigned to the F_{2g} vibrational mode for the symmetrical stretching of Ce(IV) and eight surrounding oxygens) indicate red shifts to lower wavenumber consistent with expansive strains arising from $V_O^{\bullet\bullet}$. Further, the peak positioned at ~600 cm^{-1} is attributed to the defect induced mode originating from $V_O^{\bullet\bullet}$, as previously reported [35]. The peaks at 230 cm^{-1} in Figure 5(d) is assigned to the A_{1g} vibrational mode of α-Fe_2O_3, while the peaks at 294, 395, and 620 cm^{-1} correspond to E_g vibrational modes of α-Fe_2O_3[36]. In addition, there are three peaks at 310 (T_{2g}), 538 (T_{2g}), and 680 (A_{1g}) associated with the vibrational mode of Fe_3O_4[36-37]. Figure 5(e) illustrates the coexistence of NiO (magenta color peaks) and CeO_2 (grey peaks). The peaks for E_g, one-phonon transverse optical (1T), one-phonon longitudinal optical (1L), two-phonon transverse optical (2T) vibrational mode of NiO are laid at 287, 380, 560, and 690 cm^{-1}.[38] Deconvolution of the ZCO peaks in Figure 5(f) reveals two peaks at 380 cm^{-1} and 412 cm^{-1}, which are ascribed to the A_{1T} and E_{1T} vibrational modes of ZnO. Furthermore, the peak at 580 cm^{-1} is assigned to the E_{1L} vibrational mode of ZnO[39]. Similarly, the coexistence of TMOs and CeO_{2-x} nanosheets were confirmed by XRD analysis as shown in Figure 5(g-i). Additional data analysis of the heterostructures are provided in Supplementary Figures S46.
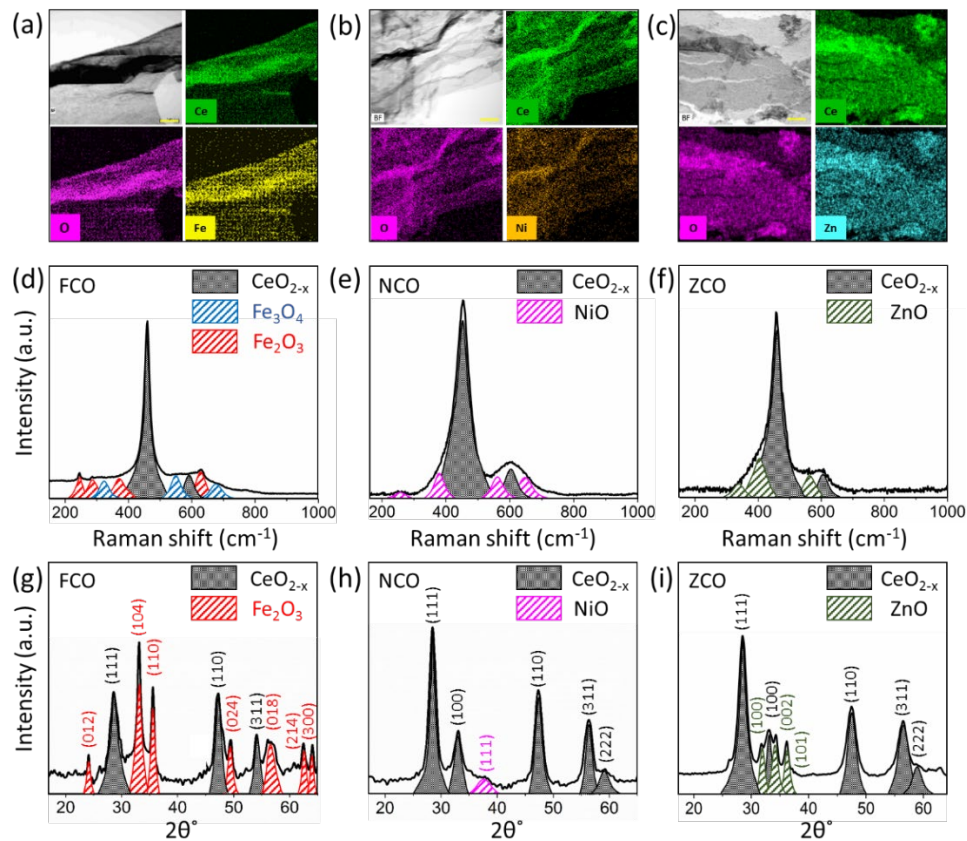

Figure 5. Characterisation of TMO heterojunction nanosheets. (a-c) TEM images of FCO, NCO, and ZCO 0D/2D heterojunctions, respectively; (d-f) EDS mapping of of FCO, NCO, and ZCO 0D/2D heterojunctions, respectively; (g-i) laser Raman microspectra of FCO, NCO, and ZCO 0D/2D heterojunctions, respectively.

In order to investigate the photocatalysis performances of CeO_{2-x} and the mixed heterojunction nanostructures, the corresponding electronic band structures were constructed. Hence XPS, UV-Vis spectrophotometry, and Kelvin probe force microscopy (KPFM) were used to determine the gaps between the valence bands (VB, orange lines), conduction bands (CB, green lines) and the Fermi levels (E_f, black dashed lines), optical indirect band gaps (E_g), and the work functions (Φ). The AFM image in Figure 6(a) illustrates the basis for the KPFM result for CeO_{2-x} shown in Figure 6(b). There is a significant difference of 90 mV (0.09 eV) potential between that of the silicon substrate (higher potential) and the deposited CeO_{2-x} nanosheet (lower potential) of 1.2 nm thickness. Since the Φ of a platinum/iridium-coated silicon tip was measured to be 4.74 eV (similar to that reported previously)[40], then subtracting 0.09 eV gives a Φ for CeO_{2-x} of 4.65 eV. The XPS plot for the valence band of CeO_{2-x} is shown in Figure 6(c), where the presence of trapping states within the bandgap is illustrated. Additionally, the Tauc plot for the E_g is shown in Figure 6(d). These data and those for FCO, NCO, and ZCO (see Supplementary Figures S47 and S48) were used to construct the electronic energy level diagrams shown in Figure 6(e).
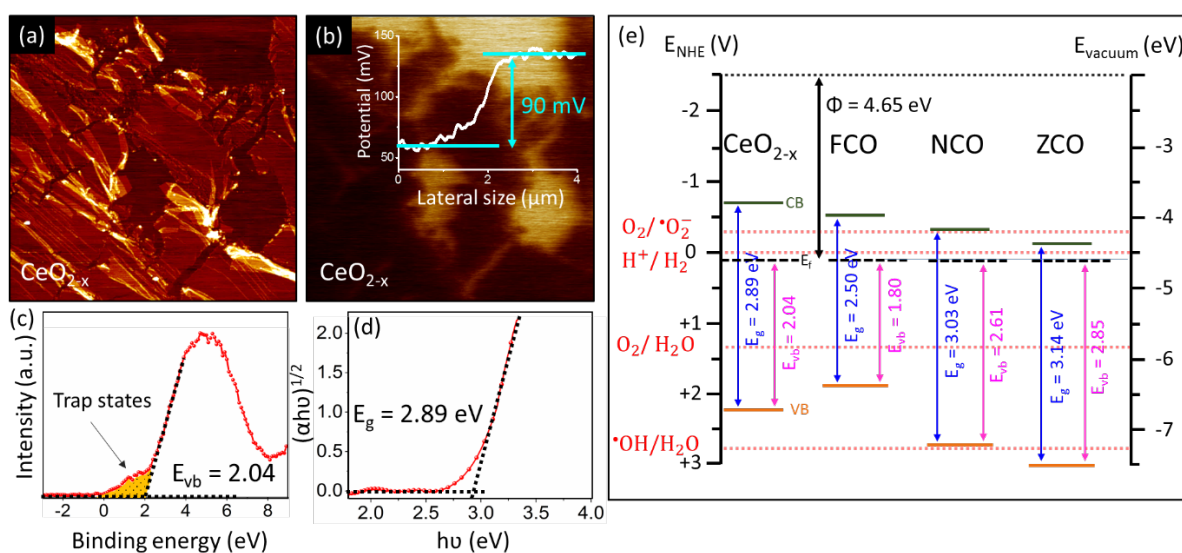

Figure 6. Band structure characterization of CeO_{2-x} and heterojunctions. (a) Topography of CeO_{2-x} holey nanosheet, (b) Contact potential difference measured by KPFM of CeO_{2-x} holey nanosheet, (c) XPS valence band plot for CeO_{2-x} holey nanosheet, (d) Tauc plot from UV-Vis spectrophotometry data for CeO_{2-x} holey nanosheet (Tauc plot model $(\alpha h\upsilon) = A(h\upsilon - E_g)^2$ applied, where A and α are absorption and absorption coefficient, respectively; $h\upsilon$ is photon energy; and E_g is optical indirect band gap), (e) electronic energy level diagram for CeO_{2-x} holey nanosheet and heterojunctions.

The preceding demonstrates that these holey 2D nanostructures offer the dual advantages of rapid charge-carrier diffusion and significant reduction in the E_g from 3.36 eV[41] to 2.89 eV. Moreover, the potential to leverage the effects of midgap trapping states (Figure 6(c)) associated with the presence of $V_O^{\bullet\bullet}$ and V_{Ce}'''' is present, although the positions of the corresponding energy levels do not appear to have been determined. Critically, Figure 6(e) demonstrates that the photocatalytic capacity for specific chemical reactions can be engineered by modification of the electronic band structure through the creation of heterojunction nanostructures. For example, Figure 6(e) shows that the Fe_2O_3/Fe_3O_4-CeO_{2-x} heterostructure (FCO) lowers the E_g to 2.50 eV and positions the CB (green line) for CeO_{2-x} above that of Fe_2O_3/Fe_3O_4 but also above the $O_2/{}^\bullet O_2^-$

energy level. The former significantly increases light absorption and the latter enhances the formation of reactive oxygen species (ROS) by enabling electron transfer from CeO_{2-x} to Fe_2O_3/Fe_3O_4, the proximity of the latter of which to the $O_2/^\bullet O_2^-$ energy level facilitates the $O_2 \rightarrow {}^\bullet O_2^-$ reaction. The VB and CB band alignments also suggest that charge transfer of both electrons and holes would be toward Fe_2O_3/Fe_3O_4, indicating that this would enhance charge recombination. However, reduced electron/hole recombination of the heterojunction relative to the CeO_{2-x} nanosheet was confirmed by PL spectroscopy (Supplementary Figure S49). Therefore, these data suggest that the charge transfer is dominated by the short diffusion distance through the thinness of the nanosheets rather than recombination at Fe_2O_3/Fe_3O_4.

XPS analyses (Supplementary Figure S47) of the NCO and ZCO heterojunctions also showed the formation of trapping states. Although the band gaps of NCO and ZCO were increased (Figure 6(e)), the CB for NCO and the VB for ZCO are positioned appropriately to effect the $O_2/^\bullet O_2^-$ and $^\bullet OH/H_2O$ reactions, respectively, thereby enhancing the respective ROS formation. Further, both the VB and CB decrease relative to those for CeO_{2-x}, indicating that charge separation would be improved by electron diffusion to the TMO and hole diffusion to the CeO_{2-x}.

The effects of band engineering on the photocatalytic performance were studied by photodegradation of methylene blue dye, as a standard for organic phase decomposition by ROS[42], through 100 mW/cm^2 of irradiance at AM 1.5 G solar illumination. While the holey CeO_{2-x} nanosheet exhibits a high dye degradation extent of 85% after 2 h (Supplementary Figure S50), the kinetics of the reaction reveal a rate constant (*k*) as high as 0.024 min^{-1}, which apparently represents fastest dye degradation by pure CeO_2 reported. The heterojunctions performed even better, which FCO, NCO, and ZCO reaching extents of 100%, 94%, and 90%, respectively, after 2 h, with correspondingly higher rate constants. The high stability of the samples were confirmed after multiple photocatalytic tests, the results of which are plotted as presented in (Supplementary Figure S51).

In summary, the present work paves the way for the fabrication of novel strategy to fabricate new class of stratified MCPs, which are exfoliated readily in water at room temperature. The exfoliation process resulted in the formation of extremely thin holey nanosheets of MOs with polycrystalline structure. The diffusion distance for charge carriers is here limited while the accessibility of active sites for catalysis reactions is maximised. Furthermore, using holey CeO_{2-x} nanosheets (2D), as template to fabricate mixed 0D/2D heterojunction structure of TMOs (0D), was shown to be a promising route to optimise photocatalysts at the nanoscale regime, by tailoring their electronic structure through rearrangement of band positions.

Data Availability

All data are available within the manuscript and supporting information. Further data can be acquired from the corresponding authors (s.seifimofarah@unsw.edu.au, adabifiroozjaei.e@nims.go.jp, koshy@unsw.edu.au) upon reasonable request.

References

[1]   C. L. Tan, X. H. Cao, X. J. Wu, Q. Y. He, J. Yang, X. Zhang, J. Z. Chen, W. Zhao, S. K. Han, G. H. Nam, M. Sindoro, H. Zhang, *Chem Rev* **2017**, *117*, 6225-6331.

[2]   J. N. Tiwari, R. N. Tiwari, K. S. Kim, *Progress in Materials Science* **2012**, *57*, 724-803.

[3]   aY. Zhu, L. Peng, Z. Fang, C. Yan, X. Zhang, G. Yu, *Advanced materials* **2018**, *30*, e1706347; bY. Xue, Q. Zhang, W. Wang, H. Cao, Q. Yang, L. Fu, *Advanced Energy Materials* **2017**, *7*, 1602684.

[4]   aD. Deng, K. S. Novoselov, Q. Fu, N. Zheng, Z. Tian, X. Bao, *Nature nanotechnology* **2016**, *11*, 218; bX. Chia, M. Pumera, *Nature Catalysis* **2018**, *1*, 909-921.

[5]   aQ. H. Wang, K. Kalantar-Zadeh, A. Kis, J. N. Coleman, M. S. Strano, *Nature nanotechnology* **2012**, *7*, 699; bV. Nicolosi, M. Chhowalla, M. G. Kanatzidis, M. S. Strano, J. N. Coleman, *Science* **2013**, *340*, 1226419; cR. Ma, T. Sasaki, *Advanced materials* **2010**, *22*, 5082-5104.

[6]   K. Varoon, X. Zhang, B. Elyassi, D. D. Brewer, M. Gettel, S. Kumar, J. A. Lee, S. Maheshwari, A. Mittal, C. Y. Sung, M. Cococcioni, L. F. Francis, A. V. McCormick, K. A. Mkhoyan, M. Tsapatsis, *Science* **2011**, *334*, 72-75.

[7]   aA. Zavabeti, J. Z. Ou, B. J. Carey, N. Syed, R. Orrell-Trigg, E. L. H. Mayes, C. Xu, O. Kavehei, A. P. O'Mullane, R. B. Kaner, K. Kalantar-zadeh, T. Daeneke, *Science* **2017**, *358*, 332-335; bN. Syed, A. Zavabeti, J. Z. Ou, M. Mohiuddin, N. Pillai, B. J. Carey, B. Y. Zhang, R. S. Datta, A. Jannat, F. Haque, K. A. Messalea, C. Xu, S. P. Russo, C. F. McConville, T. Daeneke, K. Kalantar-Zadeh, *Nature communications* **2018**, *9*, 3618; cB. J. Carey, J. Z. Ou, R. M. Clark, K. J. Berean, A. Zavabeti, A. S. R. Chesman, S. P. Russo, D. W. M. Lau, Z.-Q. Xu, Q. Bao, O. Kavehei, B. C. Gibson, M. D. Dickey, R. B. Kaner, T. Daeneke, K. Kalantar-Zadeh, *Nature communications* **2017**, *8*, 14482.

[8]   aJ. N. Coleman, M. Lotya, A. O'Neill, S. D. Bergin, P. J. King, U. Khan, K. Young, A. Gaucher, S. De, R. J. Smith, I. V. Shvets, S. K. Arora, G. Stanton, H.-Y. Kim, K. Lee, G. T. Kim, G. S. Duesberg, T. Hallam, J. J. Boland, J. J. Wang, J. F. Donegan, J. C. Grunlan, G. Moriarty, A. Shmeliov, R. J. Nicholls, J. M. Perkins, E. M. Grieveson, K. Theuwissen, D. W. McComb, P. D. Nellist, V. Nicolosi, *Science* **2011**, *331*, 568-571; bS. Z. Butler, S. M. Hollen, L. Cao, Y. Cui, J. A. Gupta, H. R. Gutiérrez, T. F. Heinz, S. S. Hong, J. Huang, A. F. Ismach, E. Johnston-Halperin, M. Kuno, V. V. Plashnitsa, R. D. Robinson, R. S. Ruoff, S. Salahuddin, J. Shan, L. Shi, M. G. Spencer, M. Terrones, W. Windl, J. E. Goldberger, *ACS nano* **2013**, *7*, 2898-2926.

[9]   J. R. Brent, N. Savjani, P. O'Brien, *Progress in Materials Science* **2017**, *89*, 411-478.

[10]   T. Rodenas, I. Luz, G. Prieto, B. Seoane, H. Miro, A. Corma, F. Kapteijn, I. X. F. X. Llabres, J. Gascon, *Nature materials* **2015**, *14*, 48-55.

[11]   D. Zhou, Y. Cui, P.-W. Xiao, M.-Y. Jiang, B.-H. Han, *Nature communications* **2014**, *5*, 4716.

[12]   aJ. Yu, Y. Wang, L. Mou, D. Fang, S. Chen, S. Zhang, *Acs Nano* **2018**, *12*, 2035-2047; bC. Wu, *Inorganic Two-dimensional Nanomaterials: Fundamental Understanding, Characterizations and Energy Applications*, Royal Society of Chemistry, **2017**.

[13]   aL. L. Peng, P. Xiong, L. Ma, Y. F. Yuan, Y. Zhu, D. H. Chen, X. Y. Luo, J. Lu, K. Amine, G. H. Yu, *Nat Commun* **2017**, *8*; bJ. Mahmood, E. K. Lee, M. Jung, D. Shin, I.-Y. Jeon, S.-M. Jung, H.-J. Choi, J.-M. Seo, S.-Y. Bae, S.-D. Sohn, N. Park, J. H. Oh, H.-J. Shin, J.-B. Baek, *Nature communications* **2015**, *6*, 6486.

[14]   Y. Xu, Z. Lin, X. Zhong, X. Huang, N. O. Weiss, Y. Huang, X. Duan, *Nature communications* **2014**, *5*, 4554.

[15]   aL. Peng, P. Xiong, L. Ma, Y. Yuan, Y. Zhu, D. Chen, X. Luo, J. Lu, K. Amine, G. Yu, *Nature communications* **2017**, *8*, 15139; bL. Peng, Z. Fang, J. Li, L. Wang, A. M. Bruck, Y. Zhu, Y. Zhang, K. J. Takeuchi, A. C. Marschilok, E. A. Stach, E. S. Takeuchi, G. Yu, *Acs Nano* **2018**, *12*, 820-828.

[16]   L. Peng, Z. Fang, Y. Zhu, C. Yan, G. Yu, *Advanced Energy Materials* **2018**, *8*, 1702179.

[17]   aZ. Fang, L. Peng, Y. Qian, X. Zhang, Y. Xie, J. J. Cha, G. Yu, *Journal of the American Chemical Society* **2018**, *140*, 5241-5247; bK. Xiang, Z. Xu, T. Qu, Z. Tian, Y. Zhang, Y. Wang, M. Xie, X. Guo, W. Ding, X. Guo, *Chemical communications* **2017**, *53*, 12410-12413.

[18]   D. Channei, S. Phanichphant, A. Nakaruk, S. Mofarah, P. Koshy, C. Sorrell, *Catalysts* **2017**, *7*, 45.

[19]   J. Zemann, *Acta Crystallographica* **1965**, *18*, 139-139.

[20]   aD. Channei, S. Phanichphant, A. Nakaruk, S. S. Mofarah, P. Koshy, C. C. Sorrell, *Catalysts* **2017**, *7*; bS. M. S, E. Adabifiroozjaei, Y. Yao, P. Koshy, S. Lim, R. Webster, X. Liu, R. Khayyam Nekouei, C. Cazorla, Z. Liu, Y. Wang, N. Lambropoulos, C. C. Sorrell, *Nature communications* **2019**, *10*, 2594.

[21]   D. Chen, L. Peng, Y. Yuan, Y. Zhu, Z. Fang, C. Yan, G. Chen, R. Shahbazian-Yassar, J. Lu, K. Amine, G. Yu, *Nano letters* **2017**, *17*, 3907-3913.

[22]   H. Hojo, T. Mizoguchi, H. Ohta, S. D. Findlay, N. Shibata, T. Yamamoto, Y. Ikuhara, *Nano letters* **2010**, *10*, 4668-4672.

[23]   aB. Feng, I. Sugiyama, H. Hojo, H. Ohta, N. Shibata, Y. Ikuhara, *Sci Rep-Uk* **2016**, *6*, 20288; bH. Hojo, T. Mizoguchi, H. Ohta, S. D. Findlay, N. Shibata, T. Yamamoto, Y. Ikuhara, *Nano Lett* **2010**, *10*, 4668-4672; cY. Lin, Z. Wu, J. Wen, K. R. Poeppelmeier, L. D. Marks, *Nano Lett* **2014**, *14*, 191-196.

[24]   aB. Huang, R. Gillen, J. Robertson, *The Journal of Physical Chemistry C* **2014**, *118*, 24248-24256; bL. Shi, E. Vathonne, V. Oison, M. Freyss, R. Hayn, *Physical Review B* **2016**, *94*, 115132.

[25]   aF. Zhang, P. Wang, J. Koberstein, S. Khalid, S.-W. Chan, *Surface Science* **2004**, *563*, 74-82; bC. M. Sims, R. A. Maier, A. C. Johnston-Peck, J. M. Gorham, V. A. Hackley, B. C. Nelson, *Nanotechnology* **2018**, *30*, 085703.

[26]   V. Stetsovych, F. Pagliuca, F. Dvorak, T. Duchon, M. Vorokhta, M. Aulicka, J. Lachnitt, S. Schernich, I. Matolinova, K. Veltruska, T. Skala, D. Mazur, J. Myslivecek, J. Libuda, V. Matolin, *J Phys Chem Lett* **2013**, *4*, 866-871.

[27]   aR. Mehmood, X. Wang, P. Koshy, J. L. Yang, C. C. Sorrell, *CrystEngComm* **2018**, *20*, 1536-1545; bR. Mehmood, S. S. Mofarah, W. F. Chen, P. Koshy, C. C. Sorrell, *Inorganic chemistry* **2019**, *58*, 6016-6027.

[28]   N. Syed, A. Zavabeti, K. A. Messalea, E. Della Gaspera, A. Elbourne, A. Jannat, M. Mohiuddin, B. Y. Zhang, G. Zheng, L. Wang, S. P. Russo, E. Dorna, C. F. McConville, K. Kalantar-Zadeh, T. Daeneke, *Journal of the American Chemical Society* **2019**, *141*, 104-108.

[29]   Springer-Verlag Berlin Heidelberg & Material Phases Data System (MPDS), Switzerland & National Institute for Materials Science (NIMS), Japan.

[30]   D. A. H. Hanaor, C. C. Sorrell, *Journal of Materials Science* **2011**, *46*, 855-874.

[31]   S. Zinatloo-Ajabshir, M. Salavati-Niasari, *Journal of Materials Science: Materials in Electronics* **2016**, *27*, 3918-3928.

[32]   C. C. Sorrell, H. Taib, T. C. Palmer, F. Peng, Z. M. Xia, M. Wei, in *Biological and Biomedical Coatings Handbook: Processing and Characterization* (Ed.: S. Zhang), Crc Press-Taylor & Francis Group, Boca Raton, **2011**, pp. 81-135.

[33]   aR. S. Datta, J. Z. Ou, M. Mohiuddin, B. J. Carey, B. Y. Zhang, H. Khan, N. Syed, A. Zavabeti, F. Haque, T. Daeneke, K. Kalantar-zadeh, *Nano Energy* **2018**, *49*, 237-246; bM. R. D. Bomio, R. L. Tranquilin, F. V. Motta, C. A. Paskocimas, R. M. Nascimento, L. Gracia, J. Andres, E. Longo, *The Journal of Physical Chemistry C* **2013**, *117*, 21382-21395.

[34]   D. Jariwala, T. J. Marks, M. C. Hersam, *Nature materials* **2016**, *16*, 170.

[35]   J. M. López, A. L. Gilbank, T. García, B. Solsona, S. Agouram, L. Torrente-Murciano, *Applied Catalysis B: Environmental* **2015**, *174-175*, 403-412.

[36]   A. M. Jubb, H. C. Allen, *ACS applied materials & interfaces* **2010**, *2*, 2804-2812.

[37]   T. George, A. K. Dutta, M. S. Islam, V. Leichner, J. Kirtley, H. Eilers, **2018**, 35.

[38]   P. Ravikumar, B. Kisan, A. Perumal, *AIP Advances* **2015**, *5*, 087116.

[39]   S. J. Chen, Y. C. Liu, C. L. Shao, R. Mu, Y. M. Lu, J. Y. Zhang, D. Z. Shen, X. W. Fan, *Advanced materials* **2005**, *17*, 586-590.

[40]   M. B. Ghasemian, M. Mayyas, S. A. Idrus-Saidi, M. A. Jamal, J. Yang, S. S. Mofarah, E. Adabifiroozjaei, J. Tang, N. Syed, A. P. O'Mullane, T. Daeneke, K. Kalantar-Zadeh, *Advanced Functional Materials* **2019**, 1901649.

[41]   M. M. Khan, S. A. Ansari, D. Pradhan, D. H. Han, J. Lee, M. H. Cho, *Industrial & Engineering Chemistry Research* **2014**, *53*, 9754-9763.

[42]   aS. A. Idrus-Saidi, J. Tang, M. B. Ghasemian, J. Yang, J. Han, N. Syed, T. Daeneke, R. Abbasi, P. Koshy, A. P. O'Mullane, K. Kalantar-Zadeh, *Journal of Materials Chemistry A* **2019**; bW. F. Chen, S. S. Mofarah, D. A. H. Hanaor, P. Koshy, H. K. Chen, Y. Jiang, C. C. Sorrell, *Inorganic chemistry* **2018**, *57*, 7279-7289; cS. Das, A. Samanta, S. Jana, *ACS Sustainable Chemistry & Engineering* **2017**, *5*, 9086-9094.

Supporting Information

Supplementary information is available in the online version of the paper.

Author Contributions

S.S.M. designed the project; undertook the majority of syntheses and characterisation, thermodynamic calculations, and data analyses; prepared the initial draft of the manuscript; and worked on all subsequent drafts of the manuscript. E.A. conducted large scale fabrication of CeO_{2-x} nanosheets and corresponding imaging; undertook TEM characterizations; contributed to crystallographic characterization, simulation, and data analysis of the Ce-CP; and worked on all drafts of the manuscript. R.P. undertook the syntheses of the Zr-CPs and Ti-CPs; their characterisation; and commented on final version of the manuscript. M.H.N.A. conducted *ab-initio* molecular dynamic simulation and related structural analysis. M.H. undertook neutron and x-ray structural characterization and related Rietveld analyses. Y.Y. conducted AFM and KPFM measurements. X.L. undertook photoluminescence measurement. M.B.G. conducted EDS imaging of heterojunction nanostructures. K.K.Z. assisted with the characterisation and data analyses and commented on the final version of the manuscript. R.M. undertook zeta potential measurements. S.B. assisted in XRD measurement and analysis of the Ce-CP structure. M.C.S. and J.A. contributed to the EELS and HAADF imaging and commented on the final versions of the manuscript. S.L. and Y.X. contributed to the TEM imaging. T.S. commented on the final version of the manuscript. H.A. assisted with the catalysis characterizations and commented on the final version of the manuscript. P.K. contributed to the data analyses and revised all drafts of the manuscript. C.C.S. worked on all drafts of the manuscript and supervised the overall project.

Conflict of Interest

The authors declare no competing interests.

Keywords

2D, ultrathin, holey nanostructure, band-alignment, photocatalysis